THE WEAKLY NONLINEAR MAGNETOROTATIONAL INSTABILITY

Clark, S.E.[1] and Oishi, J.S. [2,3]
Draft version August 31, 2016

ABSTRACT

We conduct a formal weakly nonlinear analysis of the magnetorotational instability (MRI) in a Taylor Couette flow. This is a multiscale perturbative treatment of the nonideal, axisymmetric MRI near threshold, subject to realistic radial boundary conditions. We analyze both the standard MRI, initialized by a constant vertical background magnetic field, and the helical MRI, in which the background magnetic field contains an azimuthal component. This is the first weakly nonlinear analysis of the MRI in a Taylor Couette geometry, as well as the first weakly nonlinear analysis of the helical MRI. We find that the evolution of the weakly nonlinear perturbation amplitude of the standard MRI is described by a real Ginzburg-Landau equation (GLE), while the amplitude of the helical MRI takes the form of a complex GLE. This suggests that the saturated state of the helical MRI may itself be unstable on long spatial and temporal scales.

1. INTRODUCTION

The magnetorotational instability (MRI) drives angular momentum transport and turbulence in astrophysical disks. Its discovery by Balbus & Hawley (1991; actually a rediscovery of Chandrasekhar 1960) was a breakthrough in the longstanding question of how efficient accretion can exist in the universe: that is, how matter collapsing onto a central body is able to coalesce despite the conservation of specific angular momentum. The ubiquity of astrophysical accretion disks suggests that a wide variety of systems both experience and overcome this centrifugal barrier. Furthermore, accretion proceeds even in hydrodynamically stable disks, where molecular viscosity is vastly insufficient to drive angular momentum transport (Shakura & Sunyaev 1973). The MRI is excited by weak magnetic fields in differentially rotating fluids, and since its discovery it has been widely invoked to explain accretion in protoplanetary disks (see Armitage 2010 and references therein), binary systems (), and disks around black holes (), as well as jet and wind launching (Lesur et al. 2013), dynamos, etc (cite these)

Although the MRI is broadly important to many astrophysical systems, many of its general properties, and in particular its nonlinear saturation mechanism, remain poorly understood. The diversity of astrophysical systems which may permit the MRI admits an enormous parameter space to be explored. In protoplanetary disks, for example, the behavior and evolution of the MRI may change drastically depending on the properties of the magnetic field, the disk composition, disk geometry, and so forth. Numerical simulation of realistic disk physics is currently an area of intense focus, and is enabling the study of nonideal MHD effects, disk stratification, nonequilibrium chemistry, and other complex physics that does not lend itself easily to analytic study (Fleming & Stone 2003, Bai 2011, Flock et al. 2013, Suzuki & Inutsuka 2014, to name only a few). Still, computational

costs inevitably constrain numerical approaches. MRI saturation is a complicated nonlinear problem which may depend on the assumptions and approximations adopted by simulations in nonobvious ways. Analytic methods can play a powerful role in elucidating the mechanisms responsible for MRI saturation. For instance, analytical approaches have revealed the mechanism that likely governs saturation in the "shearing box" approximation. The shearing box is an oft-invoked local approximation in which a section of a disk is represented by solving the MHD equations in an isolated region subject to shear periodic boundary conditions. The shearing box is an inexpensive computational framework, and has been widely used to study many aspects of the MRI (). However, while the MRI is a local instability, certain properties of the local problem are not generic to the global problem. In the shearing box, linear evolution is dominated by a class of MRI mode known as channel modes. These are linear modes which also happen to be exact solutions to the *nonlinear* local MRI equations. Runaway growth is avoided in this paradigm by the instability of the channel modes themselves, which are destroyed by parasitic (secondary) instabilities (Goodman & Xu 1994, Pessah 2010). The growth of parasitic modes provides a saturation avenue for channel mode-dominated flows, yet this is unlikely to be the dominant saturation mechanism in laboratory experiments or astrophysical disks, as channel modes are artificially over-prominent in the shearing box (e.g. Latter et al. 2015). Thus while the shearing box may accurately approximate many features of the global MRI, the saturation mechanism is not among them.

The theory we develop here employs realistic radial boundary conditions, and so MRI modes are global and channel modes are not present. A number of saturation mechanisms have been proposed for the MRI which do not rely on channel modes dominating the flow. The MRI feeds off of the free energy from differential rotation, and so a modification of the background shear may cause saturation (e.g. Knobloch & Julien 2005, Umurhan et al. 2007b). The MRI may transfer its free energy into the magnetic field, and saturate when the field is too strong to be susceptible to the MRI (e.g. Ebrahimi et al. 2009). The MRI may saturate differently depending on the par-

[1] Department of Astronomy, Columbia University, New York, NY
[2] Department of Astrophysics, American Museum of Natural History, New York, NY
[3] Department of Physics, SUNY Farmingdale

TABLE 1
FIDUCIAL PARAMETERS FOR MRI RUNS

	ξ	Pm	β	Ω_2/Ω_1	R_1/R_2	radial magnetic b.c.
Standard MRI	0	1.6E-6	41.2	0.121	0.33	conducting
Helical MRI	4	1E-6	1.7E-2	0.27	0.5	insulating

ticular parameter regime under investigation, and so our challenge is not only in identifying possible saturation mechanisms, but in understanding how and when each applies in different astrophysical environments.

Our investigation is astrophysically motivated, but we also intend our theory to be relevant to laboratory experiments. Several experimental efforts are attempting to observe the MRI in the laboratory, which would allow the study of a crucial astrophysical phenomenon in a controlled setting. Unfortunately, detection of the MRI has so far proven elusive. Sisan et al. 2004 claimed to detect the MRI in a spherical Couette flow, but most likely detected unrelated MHD instabilities instead (Hollerbach 2009, Gissinger et al. 2011). Most relevant to our work is the Princeton Plasma Physics Laboratory (PPPL) MRI Experiment, a liquid gallium Taylor-Couette flow exposed to an axial magnetic field (Ji et al. 2001). There has been some theoretical work designed to complement the Princeton MRI experiment involving direct simulation of the experimental conditions, much of it focused on the specific challenges in identifying MRI signatures despite apparatus-driven spurious flows (e.g. Gissinger et al. 2012). In particular, the vertical endcaps on a laboratory MRI apparatus drive meridional flows which both inhibit the excitement of MRI and obscure its detection. The Princeton MRI experiment employs split, independently rotating endcaps to mitigate these flows (Schartman et al. 2009). Our work here assumes an infinite vertical domain, an idealization that is theoretically expedient but experimentally impractical. However, our setup is designed to be an accurate treatment of the radial dimension of the flow in a Taylor Couette apparatus like the one used in the Princeton MRI experiment.

This realistic radial treatment means that we account for the curvature of the flow in a cylindrical apparatus. Many investigations of the MRI use the "narrow gap" approximation, in which the radial extent of the fluid channel is taken to be much smaller than the radius of curvature. That is, for a center channel radius r_0 bounded by inner and outer radii r_1 and r_2, respectively, the narrow gap approximation applies when $r_0 \gg (r_2 - r_1)$. The narrow gap approximation simplifies the MRI equations by excluding curvature terms, because the flow through a narrow gap can be taken to be approximately linear in ϕ, i.e. Cartesian. Previous investigations into the weakly nonlinear behavior of the MRI have used this narrow gap approximation (Umurhan et al. 2007a, Umurhan et al. 2007b, Clark & Oishi 2016a). In this work we undertake the first (to our knowledge) weakly nonlinear analysis of the MRI in the wide gap regime, where the channel width may be comparable to or larger than its distance from the center of rotation.

Because we include curvature terms, our theory is also relevant to the helical magnetorotational instability (HMRI). Discovered by Hollerbach & Rüdiger (2005), the HMRI is an overstability in which the background magnetic field is helical. The HMRI currently occu-
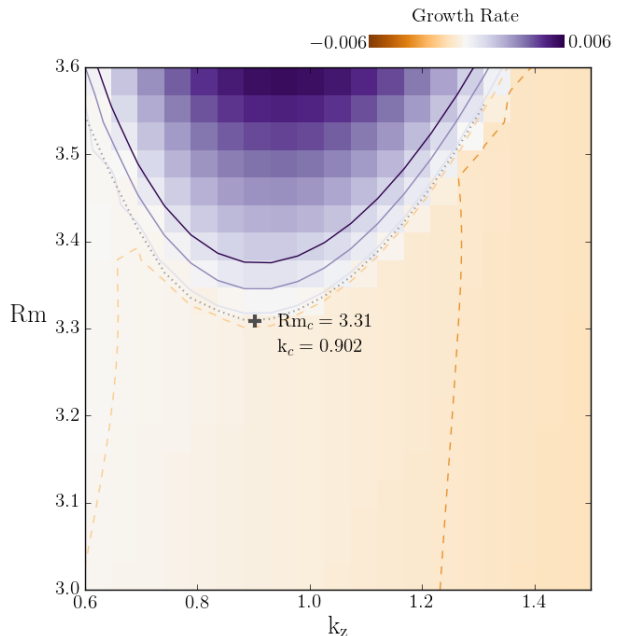

FIG. 1.— Growth rates in the (Rm, k_z) plane. Color map shows growth rate found by solving the linear eigenvalue problem for each (Rm, k_z) in the grid. The eigenvalue problem was solved for the widegap parameters listed in Table 1. Overlaid contours show growth rates at [-8E-4, -1.3E-4, 1.3E-4, 8E-4, 1.5E-3], where dashed contours represent negative values. The gray dotted line shows the interpolated marginal stability curve. The critical parameters $\mathrm{Rm}_c = 3.31$ and $k_c = 0.902$ correspond to the smallest parameter values that yield a zero growth rate.

pies a special place in the MRI puzzle. The HMRI has been proposed as a method of awakening angular momentum transport in the "dead zones" of protoplanetary disks where the magnetic Prandtl number ($Pm = \nu/\eta$) becomes very small. However the rotation profiles needed to excite HMRI may be prohibitively steeper than Keplerian depending on the boundary conditions, and so its role in astrophysical disks is currently debated (Liu et al. 2006, Rüdiger & Hollerbach 2007, Kirillov & Stefani 2013). The HMRI is significantly easier to excite in a laboratory setting than the standard MRI, and has already been detected in the laboratory by the Potsdam Rossendorf Magnetic Instability Experiment (PROMISE; Stefani et al. 2006, Stefani et al. 2009).

In this work we explore the behavior of the viscous, dissipative MRI in a cylindrical geometry close to threshold, making explicit comparisons to the standard MRI behavior in the thin-gap regime. We investigate both the standard MRI, in which the background magnetic field is purely axial, as well as the helical MRI, in which the background magnetic field has an azimuthal component as well.
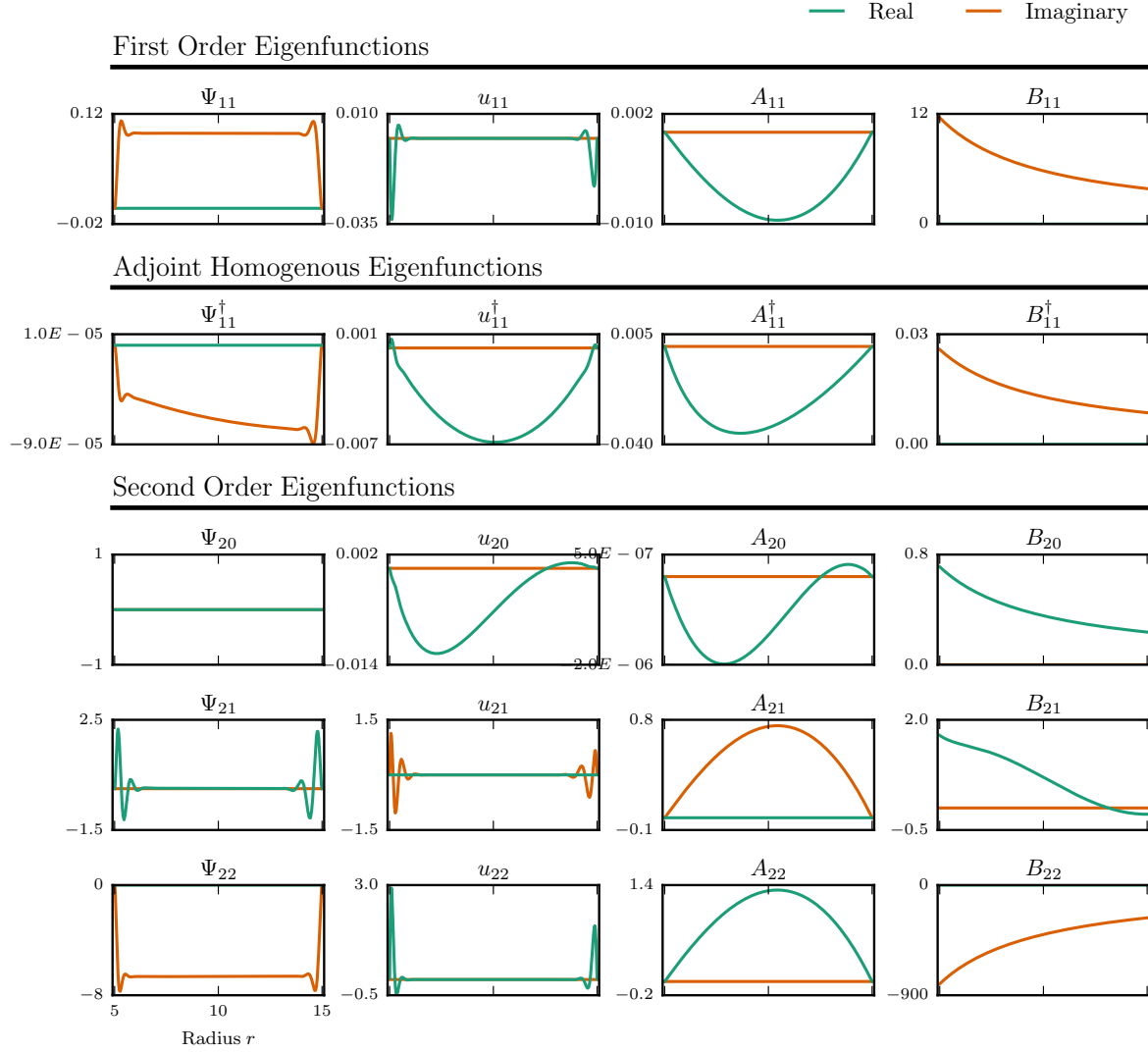
2. WIDE GAP EQUATIONS

FIG. 2.— Eigenfunctions of the first order equations, first order adjoint homogenous equations, and second order equations. We use our fiducial parameters for the standard MRI ($\xi = 0$). First-order eigenfunctions are normalized such that they are either purely real or purely imaginary, and such that $\int \Psi_{11} dr = 1$. Adjoint homogenous eigenfunctions are normalized such that $\left\langle V_{11}^{\dagger} \cdot \mathcal{D} V_{11} \right\rangle = 1$.

The basic equations solved are the momentum and induction equations,

$$\partial_t \mathbf{u} + \mathbf{u} \cdot \nabla \mathbf{u} = -\frac{1}{\rho} \nabla P - \nabla \Phi + \frac{1}{\rho} \left(\mathbf{J} \times \mathbf{B} \right) + \nu \nabla^2 \mathbf{u} \quad (1)$$

and

$$\partial_t \mathbf{B} = \nabla \times \left(\mathbf{u} \times \mathbf{B} \right) + \eta \nabla^2 \mathbf{B}, \quad (2)$$

where P is the gas pressure, ν is the kinematic viscosity, η is the microscopic diffusivity, $\nabla \Phi$ is the gravitational force per unit mass, and the current density is $\mathbf{J} = \nabla \times \mathbf{B}$. We solve these equations subject to the incompressible fluid and solenoidal magnetic field constraints,

$$\nabla \cdot \mathbf{u} = 0 \quad (3)$$

and

$$\nabla \cdot \mathbf{B} = 0. \quad (4)$$

We perturb these equations axisymmetrically in a cylindrical (r, ϕ, z) geometry, i.e. $\mathbf{u} = \mathbf{u_0} + \mathbf{u_1}$ and $\mathbf{B} = \mathbf{B_0} + \mathbf{B_1}$, where $\mathbf{u_0}$ and $\mathbf{B_0}$ are defined below. We define a Stokes stream function Ψ such that

$$\mathbf{u_1} = \begin{bmatrix} \frac{1}{r} \partial_z \Psi \ \hat{\mathbf{r}} \\ u_\phi \ \hat{\phi} \\ -\frac{1}{r} \partial_r \Psi \ \hat{\mathbf{z}} \end{bmatrix}, \quad (5)$$

and the magnetic vector potential A is

$$\mathbf{B_1} = \begin{bmatrix} \frac{1}{r} \partial_z A \ \hat{\mathbf{r}} \\ B_\phi \ \hat{\phi} \\ -\frac{1}{r} \partial_r A \ \hat{\mathbf{z}} \end{bmatrix}. \quad (6)$$

These definitions automatically satisfy Equations 3 and 4 for axisymmetric disturbances. We note that in the linearized equations, streamfunctions of the form $u_x = \partial_z \Psi$, $u_z = -(\partial_r + \frac{1}{r})\Psi$, and the corresponding definitions of the magnetic vector potential, are convenient choices, but we define Equations 5 and 6 for this nonlinear investigation because of the incommutability of ∂_r and $\partial_r + \frac{1}{r}$.

The astrophysical magnetorotational instability operates in accretion disks and in stellar interiors, environments where fluid rotation is strongly regulated by gravity. In accretion disks, differential rotation is imposed gravitationally by a central body, so the rotation profile is forced to be Keplerian. Clearly a gravitationally enforced Keplerian flow is inaccessible to laboratory study, so differential rotation is created by rotating an inner cylinder faster than an outer cylinder (a Taylor-Couette setup). For a nonideal fluid subject to no-slip boundary conditions, the base flow is

$$\Omega(r) = c_1 + \frac{c_2}{r^2}, \tag{7}$$

where $c_1 = (\Omega_2 r_2^2 - \Omega_1 r_1^2)/(r_2^2 - r_1^2)$, $c_2 = r_1^2 r_2^2 (\Omega_1 - \Omega_2)/(r_2^2 - r_1^2)$, and Ω_1 and Ω_2 are the rotation rates at the inner and outer cylinder radii, respectively. In the laboratory, r_1 and r_2 are typically fixed by experimental design. However Ω_1 and Ω_2 may be chosen such that

the flow in the center of the channel is approximately Keplerian. Defining a shear parameter q, we see that for Couette flow,

$$q(r) \equiv -\frac{d \ln \Omega}{d \ln r} = \frac{2c_2}{c_1 r^2 + c_2}. \tag{8}$$

Thus through judicious choice of cylinder rotation rates, one can set $q(r_0) = 3/2$, for quasi-Keplerian flow. Note that the narrow gap approximation imposes a linear shear (constant q), and thus the interaction of fluid perturbations with the base velocity profile differs significantly from the case considered here. Our base velocity is

$$\mathbf{u_0} = r\Omega(r)\hat{\phi}. \tag{9}$$

We initialize a magnetic field

$$\mathbf{B_0} = B_0 \hat{\mathbf{z}} + B_0 \xi \frac{r_0}{r} \hat{\phi}, \tag{10}$$

so that the base magnetic field is axial when $\xi = 0$ and otherwise helical.

In this work we will focus our findings on two fiducial parameter sets, one for the standard MRI where $\xi = 0$ and one for the helical MRI. We choose the SMRI parameters to be comparable to the case considered in Goodman & Ji 2002. The HMRI parameters were chosen to be comparable to Hollerbach & Rüdiger 2005. Our fiducial parameters are described in Table 1.

Our perturbed system is

$$\frac{1}{r}\partial_t(\nabla^2\Psi - \frac{2}{r}\partial_r\Psi) - \frac{2}{\beta}\frac{1}{r}B_0\partial_z(\nabla^2 A - \frac{2}{r}\partial_r A) - \frac{2}{r}u_0\partial_z u_\phi + \frac{2}{\beta}\frac{2}{r^2}B_0\xi\partial_z B_\phi - \frac{1}{\text{Re}}\left[\nabla^2(\frac{1}{r}\nabla^2\Psi) - \frac{1}{r^3}\partial_r^2\Psi - \frac{1}{r^4}\partial_r\Psi\right] = N^{(\Psi)} \tag{11}$$

$$\partial_t u_\phi + \frac{1}{r^2}u_0\partial_z\Psi + \frac{1}{r}\partial_r u_0\partial_z\Psi - \frac{2}{\beta}B_0\partial_z B_\phi - \frac{1}{\text{Re}}(\nabla^2 u_\phi - \frac{1}{r^2}u_\phi) = N^{(u)} \tag{12}$$

$$\partial_t A - B_0\partial_z\Psi - \frac{1}{\text{Rm}}(\nabla^2 A - \frac{2}{r}\partial_r A) = N^{(A)} \tag{13}$$

$$\partial_t B_\phi + \frac{1}{r^2}u_0\partial_z A - B_0\partial_z u_\phi - \frac{1}{r}\partial_r u_0\partial_z A - \frac{2}{r^3}B_0\xi\partial_z\Psi - \frac{1}{\text{Rm}}(\nabla^2 B_\phi - \frac{1}{r^2}B_\phi) = N^{(B)} \tag{14}$$

The righthand side of the equations contain the nonlinear terms

$$N^{(\Psi)} = -J(\Psi, \frac{1}{r^2}(\nabla^2\Psi - \frac{2}{r}\partial_r\Psi)) + \frac{2}{\beta}J(A, \frac{1}{r^2}(\nabla^2 A - \frac{2}{r}\partial_r A)) - \frac{2}{\beta}\frac{2}{r}B_\phi\partial_z B_\phi + \frac{2}{r}u_\phi\partial_z u_\phi \tag{15}$$

$$N^{(u)} = \frac{2}{\beta}\frac{1}{r}J(A, B_\phi) - \frac{1}{r}J(\Psi, u_\phi) + \frac{2}{\beta}\frac{1}{r^2}B_\phi\partial_z A - \frac{1}{r^2}u_\phi\partial_z\Psi \tag{16}$$

$$N^{(A)} = \frac{1}{r}J(A, \psi) \tag{17}$$

$$N^{(B)} = \frac{1}{r}J(A, u_\phi) + \frac{1}{r}J(B_\phi, \psi) + \frac{1}{r^2}B_\phi\partial_z\psi - \frac{1}{r^2}u_\phi\partial_z A \tag{18}$$

where J is the Jacobian $J(f, g) \equiv \partial_z f \partial_r g - \partial_r f \partial_z g$. Note that in the above, $\nabla^2 f \equiv \partial_r^2 f + \partial_z^2 f + \frac{1}{r}\partial_r f$. Equations 11 - 18 are nondimensionalized by inner cylinder quantities: lengths have been scaled by r_1, velocities by $r_1\Omega_1$, and densities by ρ_0, where ρ_0 is the constant

density. Magnetic fields are scaled by B_0, the constant strength of the initial background field; where B_0 appears in the above it is formally unity. $\Omega_1 = \Omega(r_1)$ is the rotation rate of the inner cylinder. We introduce the Reynolds number $\text{Re} = \Omega_1 r_1^2/\nu$, the magnetic Reynolds
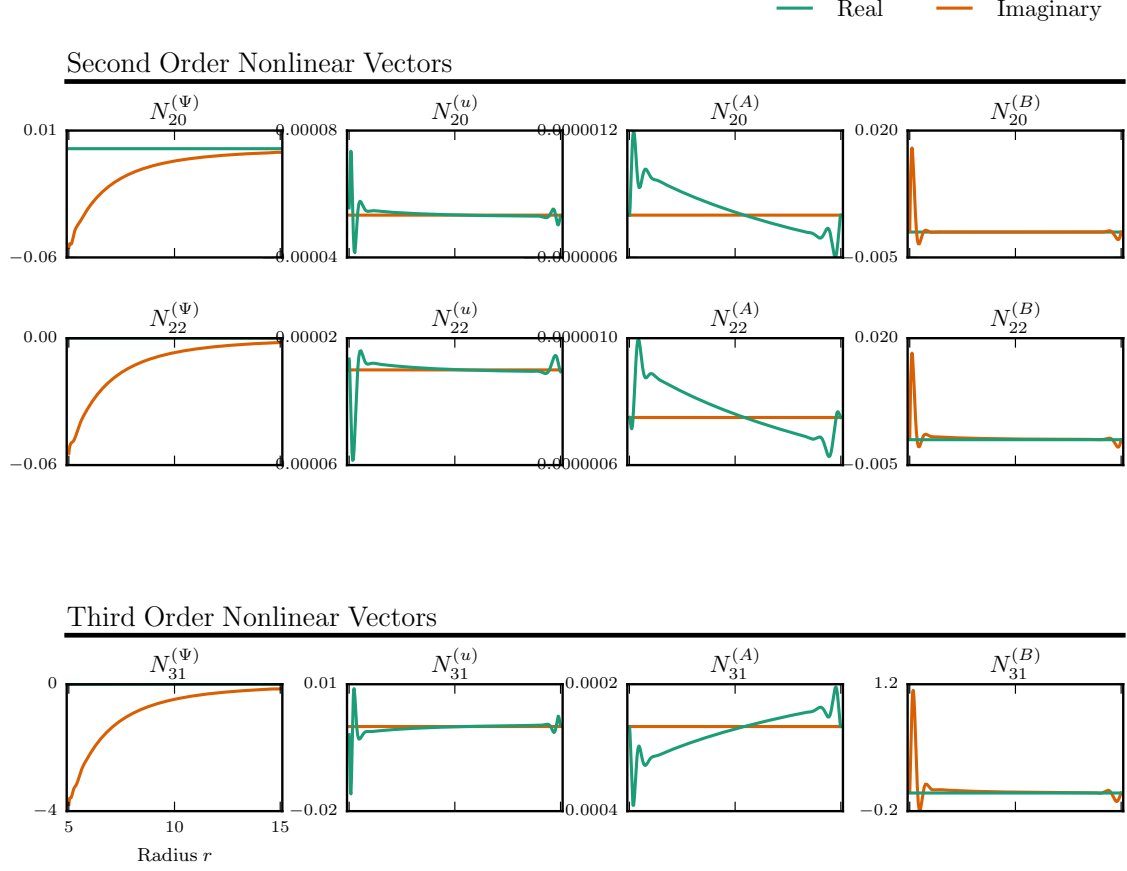
FIG. 3.— Nonlinear terms N_2 and N_3 for our fiducial standard MRI parameters.

number $\mathrm{Rm} = \Omega_1 r_1^2/\eta$, and a plasma beta parameter $\beta = \Omega_1^2 r_1^2 \rho_0/B_0^2$. Note that if we define the dimensional cylindrical coordinate $r = r_1(1+\delta x)$, we recover the narrow gap approximation of the system in the limit $\delta \to 0$.

We solve the standard MRI system subject to periodic vertical boundary conditions and no-slip, perfectly conducting radial boundary conditions, namely

$$\Psi = \partial_r\Psi = u = A = \partial_r(rB) = 0 \qquad (19)$$

at $r = r_1, r_2$. To the helical MRI system we apply insulating boundary conditions,

$$\partial_r A = k\frac{I_0(kr)}{I_1(kr)}A \text{ at } r = r_1 \qquad (20)$$

$$\partial_r A = -k\frac{K_0(kr)}{K_1(kr)}A \text{ at } r = r_2 \qquad (21)$$

and $B = 0$ at $r = r_1, r_2$ (see Willis & Barenghi 2002). Here, I_n and K_n are the modified Bessel functions of the first and second kind, respectively.

We note that Equations 11 - 14 are written in a non-standard form, with the nonlinear terms on the righthand side. This choice has a practical motivation. As detailed in §3, we expand these equations in a perturbation series and solve them order by order using a pseudospectral code. The code solves partial differential equations of the form $\mathrm{M}\partial_t\mathbf{V} + \mathrm{L}\mathbf{V} = \mathbf{F}$, where M and L are matri-
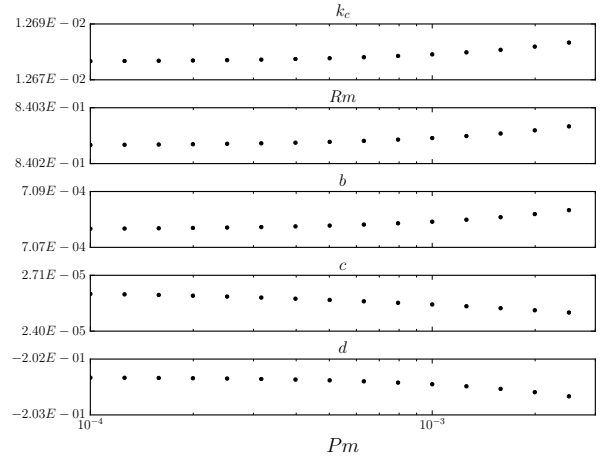

FIG. 4.— Critical parameters k_c and Rm, and coefficients of the Ginzburg-Landau equation (Equation 28) as a function of Pm. Note the very weak dependence of the coefficients on Pm. The saturation amplitude of the standard MRI system is very insensitive to Pm in the wide gap case.

ces and $\mathbf{F}$ is a vector containing any inhomogenous terms. The nonlinear terms in our perturbation analysis become inhomogenous term inputs to the solver.

3. WEAKLY NONLINEAR PERTURBATION ANALYSIS

We find the marginal system as a function of the dimensionless parameters. Marginality for
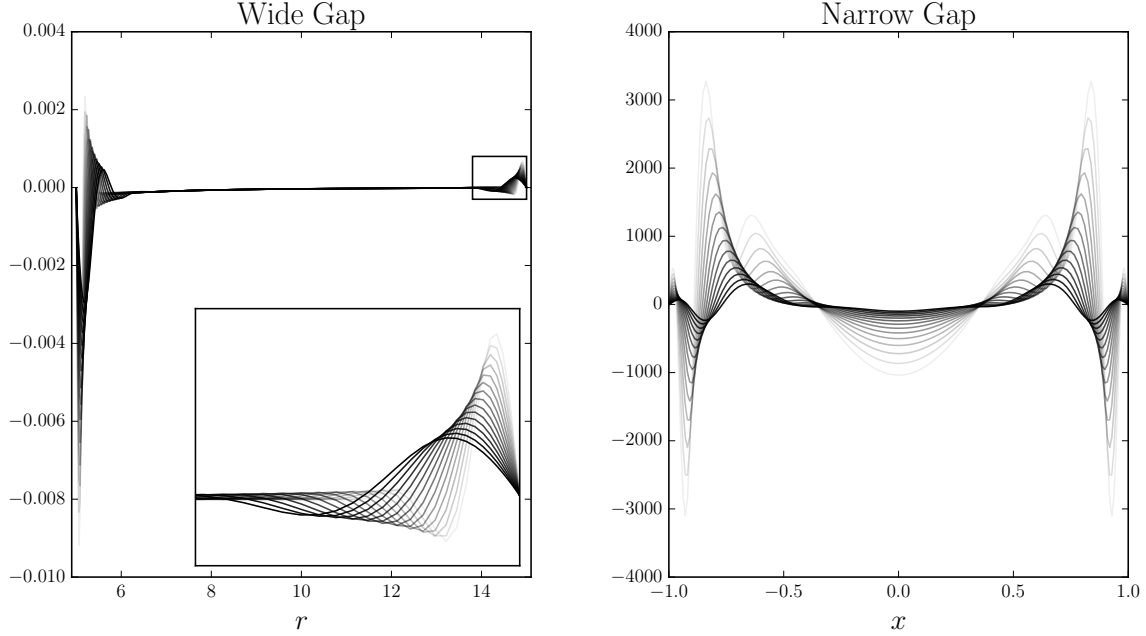
FIG. 5.— Nonlinear term $N_{31}^{(B)}$ for the wide gap (left) and narrow gap (right) standard MRI. Each line represents a run for a different Pm, from $Pm = 1E - 4$ (darkest) to $Pm \sim 1E - 3$ (lightest). Inlaid plot in wide gap case shows a zoomed-in view of the boundary layer at the outer boundary (r_2). In the narrow gap case the boundary layer strongly affects the bulk of the flow, while in the wide gap case the flow in the center of the channel is relatively unaffected by width of the boundary layers.

our standard MRI system is a hyperplane in $(\mathrm{Rm}, Pm, \beta, \Omega_2/\Omega_1, \mathrm{R}_1/\mathrm{R}_2)$, but we hold all of these constant except for Rm. To analyze the MRI system at marginality, we fix the parameters listed in Table 1 and determine the critical Rm and k_z by repeatedly solving the linear MRI system to determine the smallest parameter values for which the fastest growing mode is zero. That is, we solve the linear eigenvalue problem for eigenvalues $\sigma = \gamma + i\omega$. Figure 1 shows linear MRI growth rates γ in the (Rm, k_z) plane. For the fiducial standard MRI parameters in Table 1 we find critical parameters $\mathrm{Rm}_c = 3.30$ and $k_c = 0.901$.

Just as in the weakly nonlinear analyses of Umurhan et al. 2007b and Clark & Oishi 2016a, we tune the system away from marginality by taking $B_0 \to B_0 \left(1 - \epsilon^2\right)$, where $\epsilon \ll 1$. We parameterize scale separation as $Z = \epsilon z$ and $T = \epsilon^2 t$, where Z and T are slowly varying spatial and temporal scales, respectively. We group the fluid variables into a state vector $\mathbf{V} = [\Psi, u, A, B]^{\mathrm{T}}$, such that the full nonlinear system in Equations 11 - 18 can be expressed as

$$\mathcal{D}\partial_t\mathbf{V} + \mathcal{L}\mathbf{V} + \epsilon^2\widetilde{\mathcal{G}}\mathbf{V} + \xi\widetilde{\mathcal{H}}\mathbf{V} + \mathbf{N} = 0, \qquad (22)$$

where $\mathcal{D}$, $\mathcal{L}$, and $\widetilde{\mathcal{G}}$ are matrices defined in Appendix A, and $\mathbf{N}$ is a vector containing all nonlinear terms defined in Appendix B. We expand the variables in a perturbation series $\mathbf{V} = \epsilon\mathbf{V}_1 + \epsilon^2\mathbf{V}_2 + \epsilon^3\mathbf{V}_3 + h.o.t.$ The perturbed system can then be expressed at each order by the equations

$$\mathcal{O}(\epsilon) : \mathcal{L}\mathbf{V}_1 + \xi\widetilde{\mathcal{H}}\mathbf{V}_1 + \mathcal{D}\partial_t\mathbf{V}_1 = 0 \qquad (23)$$

$$\mathcal{O}(\epsilon^2) : \mathcal{L}\mathbf{V}_2 + \xi\widetilde{\mathcal{H}}\mathbf{V}_2 + \widetilde{\mathcal{L}}_1\partial_Z\mathbf{V}_1 + \xi\mathcal{H}\partial_Z\mathbf{V}_1 + \mathbf{N}_2 = 0 \qquad (24)$$

$$\mathcal{O}(\epsilon^3) : \mathcal{L}\mathbf{V}_3 + \xi\widetilde{\mathcal{H}}\mathbf{V}_3 + \mathcal{D}\partial_T\mathbf{V}_1 + \widetilde{\mathcal{L}}_1\partial_Z\mathbf{V}_2$$
$$+ \xi\mathcal{H}\partial_Z\mathbf{V}_2 + \widetilde{\mathcal{L}}_2\partial_Z^2\mathbf{V}_1 - \xi\widetilde{\mathcal{H}}\mathbf{V}_1 + \widetilde{\mathcal{G}}\mathbf{V}_1 + \mathbf{N}_3 = 0. \qquad (25)$$

$$(26)$$

See Appendix A for the definition of matrices and nonlinear vectors, and a thorough derivation. We emphasize that Equations 23 - 26 have the same form as these equations in the narrow gap case, although the matrices, which contain all radial derivatives, are significantly different in this wide gap formulation. This is because we do not have slow variation in the radial dimension. The slow variation in Z and T are parameterized as an amplitude function $\alpha(Z, T)$ which modulates the flow in these dimensions. This parameterization coupled with the boundary conditions lead us to an ansatz linear solution

$$\mathbf{V}_1 = \alpha(Z, T)\mathbb{V}_{11}(r)e^{ik_z z} + c.c., \qquad (27)$$

where the radial variation is contained in $\mathbb{V}_{11}$.

We solve the equations at each order using Dedalus, an open source pseudospectral code (Burns et al. in prep). We solve the radial portion of the eigenvectors on a basis of Chebyshev polynomials subject to our radial boundary conditions. We solve Equation 23 as a linear eigenvalue problem, and Equation 25 as a linear boundary value problem.

The result of the weakly nonlinear analysis is a single

amplitude equation for α. This amplitude equation is found by enforcing a solvability criterion on Equation 26. We find

$$\partial_T \alpha = b\alpha + d\partial_Z^2 \alpha - c\alpha \left| \alpha^2 \right|, \qquad (28)$$

a Ginzburg-Landau equation (GLE). The GLE governs the weakly nonlinear amplitude behavior in a wide range of physical systems, including the narrow gap MRI (Umurhan et al. 2007b), Rayleigh-Bénard convection (Newell & Whitehead 1969), and hydrodynamic Taylor Couette flow (e.g. Recktenwald et al. 1993). We emphasize that this is a model equation, valid only near marginality (e.g. Cross & Hohenberg 1993). The dynamics of the GLE are determined by its coefficients, which are in turn determined by the linear eigenfunctions and nonlinear vectors plotted in Figures 2 and 3. Equation 28 contains three coefficients: b, which determines the linear growth rate of the system, d, a diffusion coefficient, and c, the coefficient of the nonlinear term. When all of the coefficients of Equation 28 are real, this is known as the real GLE, although the amplitude α is in general complex. The real GLE is subject to several well-studied instabilities, including the Ekhaus and Zig-Zag instabilities. When the coefficients are complex, we have the complex GLE, a source of even richer phase dynamics than its real counterpart (see Aranson & Kramer 2002 for a thorough review).

4. RESULTS

4.1. *Standard MRI*

For the standard MRI we derive a real GLE. Here we note a departure from the behavior of the narrow gap system. The purely conducting boundary condition states that the axial component of the current $(\mathbf{J}_z = [\nabla \times \mathbf{B}]_z)$ must be zero at the walls. In the thin gap geometry, the purely conducting boundary condition on the azimuthal magnetic field is $\partial_x(B_y) = 0$ for axisymmetric perturbations. A spatially constant azimuthal field satisfies both the thin-gap MRI equations and this boundary condition. This neutral mode is formally included in the analysis of Umurhan et al. 2007b and yields a second amplitude equation in the form of a simple diffusion equation. This amplitude equation decouples from the GLE because of the translational symmetry of the thin-gap geometry. Because that symmetry is not preserved in the wide-gap case, Umurhan et al. postulate that slow variation in the wide-gap geometry will be governed by two coupled amplitude equations. However, the purely geometric term in Equation 14 prevents the wide-gap geometry from sustaining a neutral mode. We note that a neutral mode of the form $B_\phi(r) \propto \frac{1}{r}$ would exist in a resistance-free approximation.

The preservation of symmetries in the thin-gap geometry is worth a closer look, as its absence in the wide gap case is the source of many differences in the systems. Latter et al. 2015 point out that in the ideal limit $(\nu, \eta \to 0)$, the linearized system described by the left-hand side of Equations 11 - 14 can be expressed as a Schrödinger equation for the radial velocity. Similarly combining equations to obtain a single expression for Ψ, we find that the thin-gap limit linear ideal MRI can be expressed as

$$\partial_x^2 \Psi + k_z^2 \mathrm{U}(x)\Psi = 0 \qquad (29)$$

where $\mathrm{U}(x) = 3/v_A^2 k_z^2 + 1$ at marginality. When no-slip radial boundary conditions are applied, the thin-gap MRI system resembles a particle in a box with a radially constant potential well. Thus thin-gap linear MRI modes must be eigenstates of parity. These symmetries are preserved in the nonlinear MRI terms because they are nonlinear combinations of lower-order eigenfunctions. In the wide gap case, the "potential" $\mathrm{U}(r)$ varies with r, so symmetric and antisymmetric modes are no longer required.

The nonlinear terms, detailed in Appendix B, represent an interesting departure from the thin-gap theory. The thin-gap nonlinear terms at both second and third orders are linear combinations of Jacobians. The nonlinear terms in the wide-gap case differ from their thin-gap analogues with in the addition of vertical advective terms. These terms derive from the advective derivatives in the momentum and induction equations, but are filtered out in the thin-gap approximation. These advective terms allow the nonlinear contributions at both second and third order (i.e. N_2 and N_3) not to individually satisfy the boundary conditions on Ψ and u.

We examine the behavior of the wide gap MRI system as a function of Pm. Figure 4 shows the critical parameters k_c and Rm as a function of Pm, as well as the coefficients b, c, and d. The GLE coefficients are remarkably insensitive to Pm. From Equation 28 it is readily apparent that the asymptotic saturation amplitude is $\alpha_s = \pm\sqrt{b/c}$, so we conclude that the saturation amplitude of the MRI is only very weakly dependent on Pm. Note that because Rm is essentially constant as a function of Pm, the saturation amplitude is equivalently insensitive to Re^{-1}. This is in stark contrast to the narrow gap behavior of the system. For these same boundary conditions, Umurhan et al. (2007b) find that the narrow gap saturation amplitude scales as $Pm^{-4/3}$. They find that this amplitude dependence is driven by the $Pm^{1/3}$ dependence of the linear boundary layer. Boundary layer analysis similarly reveals a $\nu^{1/3}$ dependence for the radial extent of the boundary layer (Goodman & Ji 2002). Why does the Pm scaling of the boundary layer width not translate to a stronger Pm scaling for the saturation amplitude in the wide gap case? The boundary layer in the wide gap case is strongly localized at the walls, i.e. r_1 and r_2. Figure 5 shows the structure of the third-order nonlinear term $N_{31}^{(B)}$ as a function of Pm for both the narrow and wide gap standard MRI. N_{31} is the vector that determines the GLE coefficient c (see Appendix A for the wide gap case, and Umurhan et al. 2007b, Clark & Oishi 2016a for the narrow gap equations). Clearly, the boundary layers scale with Pm in both the wide and narrow gap MRI. However, in the narrow gap case this scaling extends prominently into the center of the channel, whereas for the wide gap case the bulk of the flow is relatively unaffected by the boundary layer scaling.

4.2. *Helical MRI*

When ξ in Equation 22 is not equal to zero, the helical MRI arises. We examine a single fiducial helical MRI
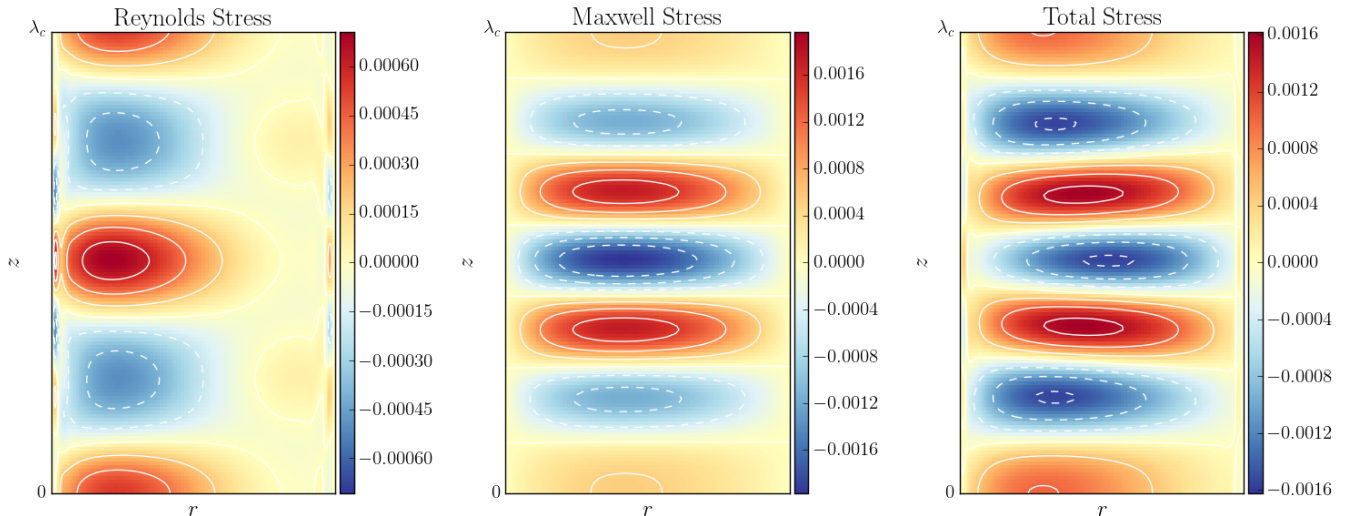
FIG. 6.— Reynolds ($\mathbb{T}_R = u_r u_\phi$), Maxwell ($\mathbb{T}_M = -\frac{2}{\beta} B_r B_\phi$), and total stress ($\mathbb{T} = \mathbb{T}_R + \mathbb{T}_M$) for the fiducial standard MRI case.

case, for the parameters listed in Table 1. At the conclusion of the weakly nonlinear analysis, we find that the coefficients of Equation 28 are $b =$, $d =$, and $c =$, i.e. complex. The marginal helical MRI is thus described by a complex GLE. This difference in character between the amplitude equations that modulate the weakly nonlinear standard and helical MRI is a consequence of the same property that makes the helical MRI an overstability. With the introduction of an azimuthal component, the background magnetic field acquires a handedness that is not present in a purely axial field.

5. DISCUSSION

Our work should be placed in the broader context of emergent pattern formation in physical systems. The real Ginzburg-Landau equation derived here governs the slow-parameter evolution of the standard MRI close to threshold. The GLE arises in a number of other physical systems, and in each case it is a consequence not of the particular physics at hand, but of the underlying symmetries in the problem. Here we make a phenomenological comparison to two other systems that give rise to a GLE. The first and perhaps most famous is Rayleigh-Bénard convection, in which a fluid between two plates is heated from below (Newell & Whitehead 1969). If we take the plane of the fluid to be infinite in the horizontal plane, the system is initially translationally symmetric. At the onset of convection the system undergoes a symmetry breaking, forming rolls, or convection cells, which break the horizontal translational invariance. Analogously, the standard MRI system considered here is initially vertically translationally symmetric, because we idealize the Taylor-Couette device as an infinitely long cylinder. The MRI breaks this symmetry, forming cells along the vertical length of the domain. Just as Rayleigh-Bénard cells transport heat vertically, the MRI cells transport angular momentum horizontally. The symmetry breaking of each of these systems is described near onset by the real GLE.

A real GLE has also been found to describe the formation of zonal flows out of magnetized turbulence in a model system (Parker & Krommes 2013). Zonal flows

are axisymmetric structures, large-scale and long-lived, which form spontaneously out of turbulence. They have recently been observed in some numerical studies of the MRI, and have generated considerable interest for their possible role in planet formation in protoplanetary disks (Johansen et al. 2009, Kunz & Lesur 2013). The present work is of course an idealized geometry, and we make no attempt to model a realistic protoplanetary disk environment. However, it is worth noting that the GLE we derive implies that axisymmetric, large-scale, long-lived structures are a generic feature of the MRI in the weakly nonlinear regime. This work provides a mathematical description of the MRI as a pattern-forming process, but much remains to be understood, particularly involving the application of this model system to realistic astrophysical disks. Our model is most directly relevant to Taylor-Couette flows, and we emphasize that laboratory MRI experiments stand poised to observe the MRI-driven pattern formation predicted here.

6. ACKNOWLEDGEMENTS

APPENDIX
A. DETAILED EQUATIONS

Here we detail the perturbation analysis described in Section 3. The linear system is described by Equation 22, where

$$\mathcal{L} = \mathcal{L}_0 + \mathcal{L}_1 \partial_z + \mathcal{L}_2 \partial_z^2 + \mathcal{L}_3 \partial_z^3 + \mathcal{L}_4 \partial_z^4, \tag{A1}$$

$$\widetilde{\mathcal{G}} = -\mathcal{G}\partial_z - \mathcal{L}_3 \partial_z^3, \tag{A2}$$

$$\widetilde{\mathcal{H}} = \mathcal{H}\partial_z, \tag{A3}$$

and the constituent matrices are defined as

$$\mathcal{L}_0 = \begin{bmatrix} -\frac{1}{\mathrm{Re}}(-\frac{3}{r^4}\partial_r + \frac{3}{r^3}\partial_r^2 - \frac{2}{r^2}\partial_r^3 + \frac{1}{r}\partial_r^4) & 0 & 0 & 0 \\ 0 & -\frac{1}{\mathrm{Re}}(\partial_r^2 + \frac{1}{r}\partial_r - \frac{1}{r^2}) & 0 & 0 \\ 0 & 0 & -\frac{1}{\mathrm{Rm}}(\partial_r^2 - \frac{1}{r}\partial_r) & 0 \\ 0 & 0 & 0 & -\frac{1}{\mathrm{Rm}}(\partial_r^2 + \frac{1}{r}\partial_r - \frac{1}{r^2}) \end{bmatrix} \tag{A4}$$

$$\mathcal{L}_1 = \begin{bmatrix} 0 & -\frac{2}{r}u_0 & \frac{2}{\beta}(\frac{1}{r^2}\partial_r - \frac{1}{r}\partial_r^2) & 0 \\ \frac{1}{r^2}u_0 + \frac{1}{r}\partial_r u_0 & 0 & 0 & -\frac{2}{\beta} \\ -1 & 0 & 0 & 0 \\ 0 & -1 & \frac{1}{r^2}u_0 - \frac{1}{r}\partial_r u_0 & 0 \end{bmatrix} \tag{A5}$$

$$\mathcal{L}_2 = \begin{bmatrix} -\frac{1}{\mathrm{Re}}(-\frac{2}{r^2}\partial_r + \frac{2}{r}\partial_r^2) & 0 & 0 & 0 \\ 0 & -\frac{1}{\mathrm{Re}} & 0 & 0 \\ 0 & 0 & -\frac{1}{\mathrm{Rm}} & 0 \\ 0 & 0 & 0 & -\frac{1}{\mathrm{Rm}} \end{bmatrix} \tag{A6}$$

$$\mathcal{L}_3 = \begin{bmatrix} 0 & 0 & -\frac{2}{\beta}\frac{1}{r} & 0 \\ 0 & 0 & 0 & 0 \\ 0 & 0 & 0 & 0 \\ 0 & 0 & 0 & 0 \end{bmatrix} \tag{A7}$$

$$\mathcal{L}_4 = \begin{bmatrix} -\frac{1}{\mathrm{Re}}\frac{1}{r} & 0 & 0 & 0 \\ 0 & 0 & 0 & 0 \\ 0 & 0 & 0 & 0 \\ 0 & 0 & 0 & 0 \end{bmatrix} \tag{A8}$$

$$\mathcal{G} = \begin{bmatrix} 0 & 0 & \frac{2}{\beta}(\frac{1}{r^2}\partial_r - \frac{1}{r}\partial_r^2) & 0 \\ 0 & 0 & 0 & -\frac{2}{\beta} \\ -1 & 0 & 0 & 0 \\ 0 & -1 & 0 & 0 \end{bmatrix} \tag{A9}$$

$$\mathcal{H} = \begin{bmatrix} 0 & 0 & 0 & \frac{2}{\beta}\frac{2}{r^2} \\ 0 & 0 & 0 & 0 \\ 0 & 0 & 0 & 0 \\ -\frac{2}{r^3} & 0 & 0 & 0 \end{bmatrix} \tag{A10}$$

$$\mathcal{D} = \begin{bmatrix} \frac{1}{r}\partial_r^2 + \frac{1}{r}\partial_z^2 - \frac{1}{r^2}\partial_r & 0 & 0 & 0 \\ 0 & 1 & 0 & 0 \\ 0 & 0 & 1 & 0 \\ 0 & 0 & 0 & 1 \end{bmatrix} \tag{A11}$$

We solve the $\mathcal{O}(\epsilon)$ (linear) system, followed by the $\mathcal{O}(\epsilon^2)$ system in Equation 25. At second order in ϵ, nonlinear terms arise which are formed by the interaction of first-order MRI modes with themselves and their complex conjugates. This mode interaction means that the second-order nonlinear term is

$$\mathbf{N}_2 = |\alpha|^2 \mathbf{N}_{20} + \alpha^2 \mathbf{N}_{22} e^{2ik_c z}, \tag{A12}$$

where terms are grouped by z-dependence. See Appendix B for the full form of the nonlinear terms. Equation 25 must therefore be solved as three separate systems of equations, one for each possible z resonance:

$$\mathcal{L}\mathbf{V}_{20} + \xi\partial_z\mathcal{H}\mathbf{V}_{20} = \mathbf{N}_{20} \tag{A13}$$

$$\mathcal{L}\mathbf{V}_{21} + \xi\partial_z\mathcal{H}\mathbf{V}_{21} = -\widetilde{\mathcal{L}}_1\partial_Z\mathbf{V}_{11} - \xi\partial_Z\mathcal{H}\mathbf{V}_{11} \tag{A14}$$

$$\mathcal{L}\mathbf{V}_{22} + \xi\partial_z\mathcal{H}\mathbf{V}_{22} = \mathbf{N}_{22} \tag{A15}$$

To find a bounded solution at $\mathcal{O}(\epsilon^3)$ we must eliminate secular terms: terms which are resonant with the solution to the linear homogenous equation $(\mathcal{L} + \xi\widetilde{\mathcal{H}})\mathbf{V} = 0$ and cause the solution to grow without bound. Secular terms in our system are those that are resonant with the linear ansatz (Equation 27), i.e. terms with e^{ik_cz} z-dependence. To eliminate these terms we enforce a solvability condition, which arises from a corollary to the Fredholm alternative. The Fredholm alternative states that if we consider a system of equations $\mathcal{L}\mathbf{V} = \mathbf{b}$ and its adjoint homogenous system $\mathcal{L}^\dagger\mathbf{V}^\dagger = 0$, only one of two conditions holds. Either there exists one and only one solution to the inhomogenous system, or the homogenous adjoint equation has a nontrivial solution. The relevant corollary arises as a consequence of the second condition: if $\mathcal{L}^\dagger\mathbf{V}^\dagger = 0$ has a nontrivial solution, then $\mathcal{L}\mathbf{V} = \mathbf{b}$ has a solution if and only if $\langle\mathbf{V}^\dagger|b\rangle = 0$.

We define the adjoint operator $\mathcal{L}^\dagger$ and solution $\mathbf{V}^\dagger$ as

$$\langle\mathbf{V}^\dagger|(\mathcal{L} + \xi\widetilde{\mathcal{H}})\mathbf{V}\rangle = \langle(\mathcal{L}^\dagger + \xi\widetilde{\mathcal{H}}^\dagger)\mathbf{V}^\dagger|\mathbf{V}\rangle, \tag{A16}$$

where the inner product is defined as

$$\langle\mathbf{V}^\dagger|\mathcal{L}\mathbf{V}\rangle = \frac{k_c}{2\pi}\int_{-\pi/k_c}^{\pi/k_c}\int_{r_1}^{r_2}\mathbf{V}^{\dagger*}\cdot\mathcal{L}\mathbf{V}\,r\mathrm{d}r\mathrm{d}z \tag{A17}$$

We derive the adjoint operator by successive integration by parts, to find

$$\mathcal{L}^\dagger = \mathcal{L}_0^\dagger - \partial_z\mathcal{L}_1^\dagger + d_z^2\mathcal{L}_2^\dagger - \partial_z^3\mathcal{L}_3^\dagger + \partial_z^4 L_4^\dagger \tag{A18}$$

and

$$\mathcal{H}^\dagger = -d_z\mathcal{H}^{\mathrm{T}}, \tag{A19}$$

where

$$\mathcal{L}_0^\dagger = \begin{bmatrix} -\frac{1}{\mathrm{Re}}\left(-\frac{3}{r^5} + \frac{3}{r^4}\partial_r - \frac{3}{r^3}\partial_r^2 + \frac{2}{r^2}\partial_r^3 + \frac{1}{r}\partial_r^4\right) & 0 & 0 & 0 \\ 0 & -\frac{1}{\mathrm{Re}}\left(\frac{1}{r}\partial_r + \partial_r^2 - \frac{1}{r^2}\right) & 0 & 0 \\ 0 & 0 & -\frac{1}{\mathrm{Rm}}\left(\frac{3}{r}\partial_r + \partial_r^2\right) & 0 \\ 0 & 0 & 0 & -\frac{1}{\mathrm{Rm}}\left(\frac{1}{r}\partial_r + \partial_r^2 - \frac{1}{r^2}\right) \end{bmatrix}, \tag{A20}$$

$$\mathcal{L}_1^\dagger = \begin{bmatrix} 0 & \frac{1}{r^2}u_0 + \frac{1}{r}\partial_r u_0 & -1 & 0 \\ -\frac{2}{r}u_0 & 0 & 0 & -1 \\ \frac{2}{\beta}\left(\frac{1}{r^3} - \frac{1}{r^2}\partial_r - \frac{1}{r}\partial_r^2\right) & 0 & 0 & \frac{1}{r^2}u_0 - \frac{1}{r}\partial_r u_0 \\ 0 & -\frac{2}{\beta} & 0 & 0 \end{bmatrix}, \tag{A21}$$

$$\mathcal{L}_2^\dagger = \begin{bmatrix} -\frac{1}{\mathrm{Re}}\left(-\frac{2}{r^3} + \frac{2}{r^2}\partial_r + \frac{2}{r}\partial_r^2\right) & 0 & 0 & 0 \\ 0 & -\frac{1}{\mathrm{Re}} & 0 & 0 \\ 0 & 0 & -\frac{1}{\mathrm{Rm}} & 0 \\ 0 & 0 & 0 & -\frac{1}{\mathrm{Rm}} \end{bmatrix}, \tag{A22}$$

and $\mathcal{L}_3^\dagger = \mathcal{L}_3^{\mathrm{T}}$, $\mathcal{L}_4^\dagger = \mathcal{L}_4^{\mathrm{T}}$. The adjoint boundary conditions are selected to satisfy Equation A17, and differ depending on the boundary conditions enforced on the homogenous system. Specifically, the boundary conditions arise from the requirement that the integrands in Equation A17 are zero at r_1 and r_2. For the conducting boundary conditions we apply to the standard MRI, the adjoint equation

$$(\mathcal{L}^\dagger + \xi\widetilde{\mathcal{H}}^\dagger)\mathbf{V}^\dagger = 0 \tag{A23}$$

must be solved subject to the boundary conditions

$$\Psi^\dagger = \partial_r\Psi^\dagger = u^\dagger = A^\dagger = \partial_r(rB^\dagger) = 0. \tag{A24}$$

For the insulating case, the adjoint boundary conditions are

$$k\frac{I_0(kr)}{I_1(kr)}rA^\dagger - 2A^\dagger - r\partial_r A^\dagger = 0 \text{ at } r = r_1 \tag{A25}$$

$$-k\frac{K_0(kr)}{K_1(kr)}rA^\dagger - 2A^\dagger - r\partial_r A^\dagger = 0 \text{ at } r = r_2 \tag{A26}$$

We take the inner product of the adjoint homogenous solution with the terms in Equation 26 that are resonant with $e^{ik_c z}$. This gives us

$$\langle\mathbb{V}^\dagger|\mathcal{D}\mathbb{V}_{11}\rangle\partial_T\alpha + \langle\mathbb{V}^\dagger|\widetilde{\mathcal{G}}\mathbb{V}_{11} - \xi\widetilde{\mathcal{H}}\mathbb{V}_{11}\rangle\alpha + \langle\mathbb{V}^\dagger|\widetilde{\mathcal{L}}_1\mathbb{V}_{21} + \widetilde{\mathcal{L}}_2\mathbb{V}_{11} + \xi\mathcal{H}\mathbb{V}_{21}\rangle\partial_Z^2\alpha = \langle\mathbb{V}^\dagger|\mathbf{N}_{31}\rangle\alpha|\alpha|^2, \tag{A27}$$

or Equation 28, the Ginzburg-Landau Equation, where the coefficients are

$$b = \langle\mathbb{V}^\dagger|\widetilde{\mathcal{G}}\mathbb{V}_{11} - \xi\widetilde{\mathcal{H}}\mathbb{V}_{11}\rangle/\langle\mathbb{V}^\dagger|\mathcal{D}\mathbb{V}_{11}\rangle, \tag{A28}$$

$$h = \langle\mathbb{V}^\dagger|\widetilde{\mathcal{L}}_1\mathbb{V}_{21} + \widetilde{\mathcal{L}}_2\mathbb{V}_{11} + \xi\mathcal{H}\mathbb{V}_{21}\rangle/\langle\mathbb{V}^\dagger|\mathcal{D}\mathbb{V}_{11}\rangle, \tag{A29}$$

and

$$c = \langle\mathbb{V}^\dagger|\mathbf{N}_{31}\rangle/\langle\mathbb{V}^\dagger|\mathcal{D}\mathbb{V}_{11}\rangle. \tag{A30}$$

B. NONLINEAR TERMS

Here we detail the perturbative expansion of the nonlinear vector $\mathbf{N}$ in Equation 22.

$$\mathbf{N} = \epsilon^2\mathbf{N}_2 + \epsilon^3\mathbf{N}_3 \tag{B1}$$

$$N_2^\Psi = J(\Psi_1, \frac{1}{r^2}\nabla^2\Psi_1) + J(\Psi_1, -\frac{2}{r^3}\partial_r\Psi_1) - \frac{2}{\beta}J(A_1, \frac{1}{r^2}\nabla^2 A_1) - \frac{2}{\beta}J(A_1, -\frac{2}{r^3}\partial_r A_1) - \frac{2}{r}u_1\partial_z u_1 + \frac{2}{\beta}\frac{2}{r}B_1\partial_z B_1 \tag{B2}$$

$$N_2^u = \frac{1}{r}J(\Psi_1, u_1) - \frac{1}{r}\frac{2}{\beta}J(A_1, B_1) + \frac{1}{r^2}u_1\partial_z\Psi_1 - \frac{2}{\beta}\frac{1}{r^2}B_1\partial_z A_1 \tag{B3}$$

$$N_2^A = -\frac{1}{r}J(A_1, \Psi_1) \tag{B4}$$

$$N_2^B = -\frac{1}{r}J(A_1, u_1) - \frac{1}{r}J(B_1, \Psi_1) - \frac{1}{r^2}B_1\partial_z\Psi_1 + \frac{1}{r^2}u_1\partial_z A_1 \tag{B5}$$

$$\begin{aligned}
N_3^\Psi &= J(\Psi_1, \frac{1}{r^2}\nabla^2\Psi_2) + J(\Psi_2, \frac{1}{r^2}\nabla^2\Psi_1) + 2J(\Psi_1, \frac{1}{r^2}\partial_Z\partial_z\Psi_1) + J(\Psi_1, -\frac{2}{r^3}\partial_r\Psi_2) + J(\Psi_2, -\frac{2}{r^3}\partial_r\Psi_1) \\
&+ \widetilde{J}(\Psi_1, \frac{1}{r^2}\nabla^2\Psi_1) + \widetilde{J}(\Psi_1, -\frac{2}{r^3}\partial_r\Psi_1) - \frac{2}{\beta}J(A_1, \frac{1}{r^2}\nabla^2 A_2) - \frac{2}{\beta}J(A_2, \frac{1}{r^2}\nabla^2 A_1) - \frac{4}{\beta}J(A_1, \frac{1}{r^2}\partial_Z\partial_z A_1) \\
&- \frac{2}{\beta}J(A_1, -\frac{2}{r^3}\partial_r A_2) - \frac{2}{\beta}J(A_2, -\frac{2}{r^3}\partial_r A_1) - \frac{2}{\beta}\widetilde{J}(A_1, \frac{1}{r^2}\nabla^2 A_1) - \frac{2}{\beta}\widetilde{J}(A_1, -\frac{2}{r^3}\partial_r A_1) \\
&- \frac{2}{r}u_1\partial_z u_2 - \frac{2}{r}u_2\partial_z u_1 - \frac{2}{r}u_1\partial_Z u_1 + \frac{2}{\beta}\frac{2}{r}B_1\partial_z B_2 + \frac{2}{\beta}\frac{2}{r}B_2\partial_z B_1 + \frac{2}{\beta}\frac{2}{r}B_1\partial_Z B_1
\end{aligned} \tag{B6}$$

$$\begin{aligned}
N_3^u &= \frac{1}{r}J(\Psi_1, u_2) + \frac{1}{r}J(\Psi_2, u_1) + \frac{1}{r}\widetilde{J}(\Psi_1, u_1) - \frac{1}{r}\frac{2}{\beta}J(A_1, B_2) - \frac{1}{r}\frac{2}{\beta}J(A_2, B_1) - \frac{1}{r}\frac{2}{\beta}\widetilde{J}(A_1, B_1) \\
&+ \frac{1}{r^2}u_1\partial_z\Psi_2 + \frac{1}{r^2}u_2\partial_z\Psi_1 + \frac{1}{r^2}u_1\partial_Z\Psi_1 - \frac{2}{\beta}\frac{1}{r^2}B_1\partial_z A_2 - \frac{2}{\beta}\frac{1}{r^2}B_2\partial_z A_1 - \frac{2}{\beta}\frac{1}{r^2}B_1\partial_Z A_1
\end{aligned} \tag{B7}$$

$$N_3^A = -\frac{1}{r}J(A_1, \Psi_2) - \frac{1}{r}J(A_2, \Psi_1) - \frac{1}{r}\widetilde{J}(A_1, \Psi_1) \tag{B8}$$

$$\begin{aligned}
N_3^B &= -\frac{1}{r}J(A_1, u_2) - \frac{1}{r}J(A_2, u_1) - \frac{1}{r}\widetilde{J}(A_1, u_1) - \frac{1}{r}J(B_1, \Psi_2) - \frac{1}{r}J(B_2, \Psi_1) - \frac{1}{r}\widetilde{J}(B_1, u_1) \\
&- \frac{1}{r^2}B_1\partial_z\Psi_2 - \frac{1}{r^2}B_2\partial_z\Psi_1 - \frac{1}{r^2}B_1\partial_Z\Psi_1 + \frac{1}{r^2}u_1\partial_z A_2 + \frac{1}{r^2}u_2\partial_z A_1 + \frac{1}{r^2}u_1\partial_Z A_1
\end{aligned} \tag{B9}$$

REFERENCES

Aranson, I.S. & Kramer, L., 2002, Rev. Mod. Phys. 74, 99

Armitage, P. 2010, ARA&A, 49, 195

Bai, X. 2011, ApJ 739, 50

Balbus, S A and Hawley, J F, 1991, The Astrophysical Journal, 376, 214

Chandrasekhar, S. 1960, Proceedings of the National Academy of Sciences of the United States of America, 46, 253

Clark, S.E. and Oishi, J.S., 2016, in prep

Cross, M. C., & Hohenberg, P. C., 1993, Rev. Mod. Phys. 65, 851

Ebrahimi, F., Prager, S.C., Schnack, D.D

Fleming, T. & Stone, J. 2003, ApJ 585, 908

Flock, M., Fromang, S., González, M., Commerçon, B. A&A 560, A43

Gissinger, C, Ji, H, Goodman, J, 2011, Phys. Rev. E 84, 026308

Gissinger, C, Goodman, J, & Ji, H, 2012, Physics of Fluids 24, 074109

Goodman, J. & Ji, H., 2002, JFM, 462, 365

Goodman, J, Xu, G, 1994, ApJ, 432, 213

Hollerbach, R, Proc. R. Soc. A, 2009, 465, 2107

Hollerbach, R. & Rüdiger, G., 2005, Phys. Rev. Lett. 95, 124501

Ji, H, Goodman, J, Kageyama, A, Mon. Not. R. Astron. Soc., 2001, 325, 1

Johansen, A., Youdin, A., Klahr, H., 2009, ApJ 697, 1269

Kirillov, O, & Stefani, F, 2013, Phys. Rev. Lett. 111, 061103

Knobloch, E, Julien K, 2005, Physics of Fluids, 17, 094106

Kunz, M.W. & Lesur, G., 2013, MNRAS 434, 2295

Latter, H.N., Fromang, S., & Faure, J., 2015, MNRAS 453, 3257

Lesur, G., Ferreira, J., & Ogilvie, G. I. 2013, A&A 550, A61

Liu, W, Goodman, J, Herron, I, and Ji, H, 2006, Phys. Rev. E 74, 056302

Newell, A.C. & Whitehead, J.A., 1969, JFM 38, 279

Parker, J.B. & Krommes, J.A., 2013, Phys of Plasmas 20, 100703

Pessah, M, 2010, ApJ, 716, 1012

Recktenwald, A., Lücke, M., Müller, H.W., 1993, Phys Rev E 48, 4444

Rüdiger, G, & Hollerbach, R, Phys. Rev. E 76, 068301

Schartman, E, Ji, H, Burin, M J, Rev Sci Instrum, 2009, 80, 024501

Shakura, N I and Sunyaev, R A, Astronomy & Astrophysics, 1973, 24, 337

Sisan, D R, Mujica, N, Tillotson, W A, Huang Y-M, Dorland, W, Hassam, A B, Antonsen, T M, Lathrop, D P, Phys Rev Lett, 2004, 93, 11

Stefani, F, Gundrum, T, Gerbeth, G, Rüdiger, G, Schultz, M, Szklarski, J, Hollerbach, R, Phys Rev Lett, 2006, 97, 184502

Stefani, F, Gerbeth, G, Gundrum, T, Hollerbach, R, Priede, J, Rüdiger, G, and Szklarski, J, Phys Rev E, 80, 066303

Suzuki, T.K. & Inutsuka, S. 2014, ApJ 784, 121

Umurhan, O.M., Regev, O., Menou, K., 2007, Phys. Rev. Letters, 98, 034501

Umurhan, O.M., Regev, O., Menou, K., 2007, Phys. Rev. E, 76, 036310

Willis, A.P. & Barenghi, C.F. 2002, JFM 463, 361